A MEMS Self-Powered Sensor and RF Transmission Platform for WSN Nodes

Cairan He, Michail E. Kiziroglou, *Member, IEEE*, David C. Yates, *Member, IEEE*, and Eric M. Yeatman, *Senior Member, IEEE*

***Abstract*—We report a new microelectromechanical systems (MEMS) self-powered sensor and RF transmission platform for wireless sensor network (WSN) nodes which can operate at energy levels orders of magnitude lower than current equivalent systems. Using the microgenerator as a power amplifier to drive a passive kick-and-resonate transmitter architecture as an alternative to a standard power hungry transmitter, this platform eliminates the need for both secondary energy storage and power conditioning circuits. This enables a significant reduction in the size, weight, complexity and cost, and allows operation at much lower excitation frequencies. The prototype platform consists of a MEMS rolling-rod microgenerator, the output voltage of which is used to kick a resonant loop antenna. The generator can be directly primed by a suitable voltage-output sensor. This is the first platform to achieve wireless sensor transmission powered only by a MEMS energy harvester.**

***Index Terms*—Capacitive, electrostatic, energy harvesting, kick-and-resonate transmitter, loop antenna, microgenerator, wireless sensor network (WSN) platform.**

I. Introduction

MINIATURIZED wireless sensor nodes capable of long-term maintenance-free operation are key to the success of wireless sensor networks (WSNs) in many diverse applications, ranging from personalized continuous health monitoring to improved water quality control [1]. The WSN approach relies on the sensor nodes being embedded into their environment, which for health applications includes being worn by or even implanted in the user. This often places stringent constraints not only on size and weight but also on power consumption, since it may be highly impractical to regularly replace or recharge embedded or implanted batteries, especially if there are many nodes forming a network. Much research effort in recent years has been devoted to the promising alternative of harvesting ambient energy as a potentially inexhaustible source of power for wireless sensor nodes. At the same time, the aim has been the miniaturization of a single node to a volume of 1 cm^3 [2].

Manuscript received April 14, 2011; accepted June 07, 2011. Date of publication June 23, 2011; date of current version November 02, 2011. This work was supported by the U.K. Engineering and Physical Sciences Research Council. The associate editor coordinating the review of this paper and approving it for publication was Prof. Okyay Kaynak.

C. He was with the Department of Electrical and Electronic Engineering, Imperial College London, London, U.K. He is now with the Institute of Microelectronics, Singapore 117685, Singapore (e-mail: hecairan@googlemail.com).

M. Kiziroglou, D. Yates, and E. Yeatman are with the Department of Electrical and Electronic Engineering, Imperial College London SW7 2AZ, U.K. (e-mail: m.kiziroglou@imperial.ac.uk; david.yates@imperial.ac.uk; e.yeatman@imperial.ac.uk).

Color versions of one or more of the figures in this paper are available online at http://ieeexplore.ieee.org.

Digital Object Identifier 10.1109/JSEN.2011.2160535

A diverse range of harvesting devices have been and are being developed both at the research and commercialisation stage, exploiting ambient light, motion, heat and electromagnetic radiation. Thermo life [3], a thermoelectric converter and a product of Thermo Life Energy Corporation, provides 30 μW at 3 V when the temperature difference between the top and bottom of the generator is only 5 K. Kuehne *et al.* [4] harvest energy from fluid flow using a piezoelectric MEMS device. Wang *et al.* [5] describe an electromagnetic generator to harness the vibration from liquid flow in a channel. The magnet is mounted on a polyethylene (PE) diaphragm which vibrates due to the pressure change in the channel. An output of 0.4 μW is achieved for the device operating at 30 Hz. Cantilever shaped piezoelectric energy harvesters, with a mass attached to the free end, were studied in great detail by Roundy *et al.* [6]. Electromagnetic energy harvesters with magnets mounted on the free end of a cantilever beam were investigated by researchers from Southampton University, U.K. [7], [8].

The microgenerator developed as part of this wireless sensor platform harvests energy from motion, considered the most versatile and ubiquitous ambient energy source available [9]. A thorough review of motion-based energy harvesting techniques using performance metrics to compare state-of-the-art devices with the theoretical limits can be found in [9], in which it was shown that the maximum power that can be generated is proportional to volume$^{4/3}$ and to frequency^3. The devices published in the literature to date generally operate at well below the theoretical maximum for the volume and the source characteristics. Although there is significant variation in the power densities achieved, it can, in general, be concluded that devices less than 1 cm^3 do not normally produce more than tens of μWs, e.g., [10] and [11]. As the frequency lowers to less than 20 Hz the power output drops to less than 10 μW, e.g., [12]–[14].

The architecture of a conventional wireless sensor node is shown in Fig. 1(a). The concept of energy harvesting envisages that the power source will be provided by a microgenerator rather than a battery. Normally, the microgenerator has to provide power for an ADC, a microprocessor, system control circuits, power management systems, and most importantly in terms of power, a radio transmitter. The low-power state-of-the-art MSP430 microcontroller from Texas Instruments requires 0.9 mW when active [15], and low-power RF radios normally dominate the power consumption of the node, demanding well above 1 mW [16].

There is then a serious shortfall in the power available from miniaturized motion-driven microgenerators when compared with the power required for the operation of a conventional wireless sensor node, especially at low excitation frequencies (the power generated is, in practice, at least a factor 10^3 less

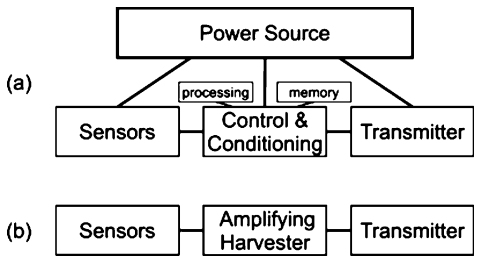

Fig. 1. Block diagram of (a) a conventional WSN node architecture and (b) the novel architecture for a WSN node.

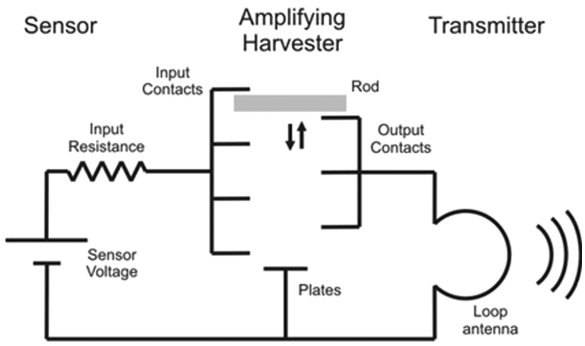

Fig. 2. Architecture of the self-powered RF transmission platform.

than the continuous power consumption, for excitation frequencies <10 Hz and total node size <1 cm^3). Approaches to overcoming this power shortage include operating at extremely low duty cycles (less than 0.1%), which is suitable for low data rate applications, the development of new ultra-low-power circuits and systems, e.g., [16], and improving microgenerator design. In order to perform duty-cycling, wireless sensor nodes employing energy harvesting still require a rechargeable battery or super-capacitor for energy storage [17], limiting the possibility for miniaturization. Smaller device volumes and lower excitation frequency operation (<10 Hz) are both desirable for certain applications such as human body sensors, which increases this energy gap still further. The approach of duty-cycling is limited not only by the requirement for secondary storage but also by the power consumption of those functions that are not switched off, e.g., the system clock. For instance, the MSP430 consumes 1.8 μW in standby which is already demanding for a sub cm^3, sub 10 Hz microgenerator.

A new architecture, shown in Fig. 1(b), for a self-powered MEMS wireless sensor platform is presented in this paper which reduces the energy requirement to only that needed to drive an antenna with the necessary power for successful data transmission. This is achieved by employing the microgenerator not as a standard battery-replacement power source for the conventional wireless sensor node shown in Fig. 1(a), but instead as a power amplifier. In this configuration the microgenerator is primed by the voltage output of the sensor; it amplifies this voltage by a constant gain and then directly drives a passive resonant antenna with this amplified output voltage. In this way, the energy to be harvested per discharge needs only to be that required to drive an antenna with the power for successful short-range transmission, which at distances of 1 m or less is sub-μW levels [18]. This means that just 1 pJ of harvested energy transmitted wirelessly over a discharge pulse time of 1 μs would enable successful operation of the sensor node (-30 dBm transmit power). The advantage can be seen if directly compared to the conventional alternative shown in Fig. 1(a). Assume that the electronic components including the radio of a conventional wireless sensor node consume 1 mW and the low-power radio achieves a maximum bit rate of 100 kbit/s: these are typical values for a design optimized for low power. With appropriate duty-cycling the energy used to transmit 1 measurement with 10 bit resolution will be 100 nJ—this is 10^5 times larger than the energy needed for the transmission of one measurement using the architecture reported here. By using the microgenerator in this novel role miniaturization can be driven far beyond that which would otherwise be possible and/or the excitation frequency at which the sensor node would be able to successfully operate could be much lower.

A significant contribution to the size of a self-powered wireless sensor node is the need for secondary energy storage such as a rechargeable battery or supercapacitor to allow duty-cycling of the electronics for reduced average power consumption. This need is entirely eliminated with the new architecture, since not only is duty-cycling not required, but nor is a separate voltage source for priming, thus further aiding miniaturization. Also, the challenges associated with designing efficient power electronics (see [9] for details) are avoided. The size, weight, cost and complexity of the wireless sensor node is hence reduced to the essential components—the sensor, the microgenerator and the antenna.

The device presented in this paper offers a proof-of-concept by demonstrating that a MEMS harvester of volume 0.2 cm^3 can indeed provide enough power at sub-10 Hz excitation frequencies for successful wireless transmission of sensed data using the new architecture. The prototype consists specifically of a rolling-rod Coulomb force parametric generator (CFPG), a loop antenna and a thermopile sensor. The new approach can, however be applied to a wide-range of microgenerator architectures, resonant antennas and voltage output sensors.

A detailed description of the basic architecture of the prototype platform is presented in Section II along with the microgenerator design and requirements. Section III will discuss generator optimization, and Section IV presents some details of the MEMS fabrication process. The measured results of the generator and complete energy harvesting wireless transmission platform are presented in Section V. Benefits and limitations of the architecture are discussed in Section VI, pointing the way to further research challenges.

II. Architecture Description

In this architecture, the sensor or sensor array primes the harvester, which then amplifies this voltage and, on discharge, kicks a passive LC transmitter, which resonates at a frequency determined by the inductive loop antenna in parallel with the harvester output capacitance. The transmitted signal amplitude is directly proportional to the measured voltage and can be received by a suitable radio. The architecture is further illustrated in Fig. 2.

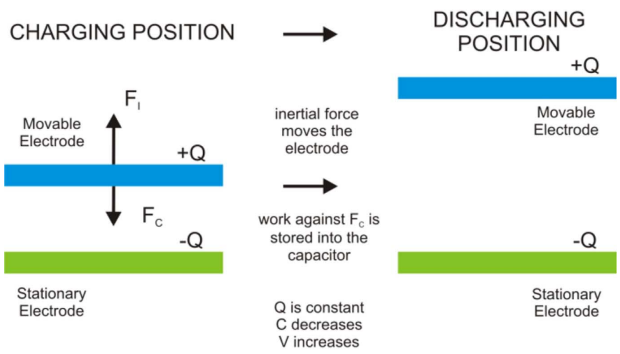

Fig. 3. Schematic description of energy harvesting operation for CFPGs.

A key component of the architecture is the inertial microgenerator, in this case designed for the particularly challenging application area of body sensor networks. The prototype flexible substrate rolling rod harvester, which has been introduced recently by the authors [19], falls into the category of CFPGs, which have been shown to be an optimal choice for the low and variable frequency and large amplitude source characteristics typical in body applications [20].

Fig. 3 illustrates the concept of a CFPG using a parallel plate capacitor. The generator consists essentially of a variable capacitor in which one plate is attached to, or forms, a proof mass, while the other is fixed to the inertial frame. A priming voltage is required to charge the capacitor at the position of maximum capacitance, labeled the charging position in Fig. 3, which is when the distance between the plates is a minimum. The charge, Q, provides the Coulomb force against which work is done as the moving plate (proof mass) travels upwards away from the fixed plate during vertical acceleration (e.g., shaking) of the inertial frame. During motion the stationary plate is held at the ground potential, whereas the moving plate is electrically isolated. Due to conservation of charge, the voltage increases as the capacitance between the plates decreases ($V = Q/C$), and hence the stored energy ($1/2Q^2/C$) also increases. The generated voltage is discharged into the load electronics at the point of minimum capacitance which corresponds to the maximum plate displacement and is the point at which the most energy is available. Kinetic energy is thus converted into electrical energy enabling the powering of electronic circuits from vibration.

Fig. 4 shows the harvester used in this work. It is a variant of the CFPG structure which possesses several advantages over the parallel plate implementation shown in Fig. 3 and explained above. The principle of operation is essentially the same. In this case, however, a conductive rod forms the proof mass and moving electrode, with the counter-electrode formed by a narrow planar strip coated with a thin dielectric. Amplification of the priming voltage is achieved as the rod rolls in-plane away from the ground plate (position of maximum capacitance) towards the discharge contact, which is centred between two ground plates (position of minimum capacitance). This geometry allows a larger proof mass than for an integrated planar device, and a larger relative displacement than for the geometry of Fig. 3. Also, multiple generation cycles can

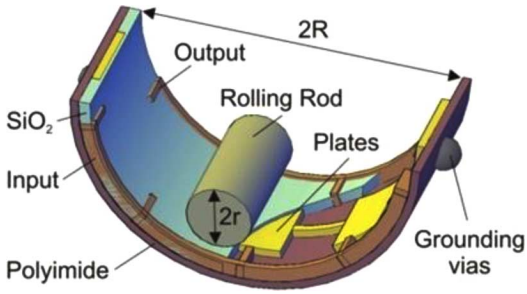

Fig. 4. Three-dimensional model of the energy harvester.

be achieved for a single movement of the rod in one direction by using multiple charge (input) and discharge (output) contacts along with multiple ground plates, as illustrated in Fig. 4. A curved substrate is used to restrict the motion of the free-moving rod. The input contacts are shown at the front of Fig. 4 where the priming voltage is applied, while the output contacts from which the amplified voltage is extracted are at the rear. Through-film bonding is employed to facilitate electrical connections (grounding vias in Fig. 4.).

The possibility of having multiple charge-discharge cycles per transit of the rod has three main advantages. Generally, a larger number of lower voltage output impulses are easier to deal with if conversion to a DC output is required. If the pulse output is used directly as is the case here, a sensor ID code can be implemented by altering the spacing between discharge contacts, thus allowing a receiver to distinguish between sensor nodes. Furthermore, some charge-discharge cycles could be used to transmit a known reference voltage, in order to deal with path-loss variation by enabling the receiver to calibrate with respect to the reference.

The amount of energy converted from mechanical form to electrical form is simply equal to the energy gained in the capacitor

$$\Delta E = \frac{1}{2}Q^2\left(\frac{1}{C_{\min}} - \frac{1}{C_{\max}}\right). \tag{1}$$

The charge Q is equal to the product of the priming voltage and the maximum capacitance. Substituting Q in (1), we obtain

$$\Delta E = \frac{1}{2}V_{\text{pri}}^2\frac{C_{\max}}{C_{\min}}(C_{\max} - C_{\min}). \tag{2}$$

The priming voltage V_{pri} is determined by the sensor. The designer of the energy harvester should therefore seek to maximize $C_{\max}$, and minimize $C_{\min}$, while ensuring that the latter remains comfortably above the parasitic capacitance.

It should be noted that the time needed to charge the generator ($\ll 10^{-8}$ s) is orders of magnitude less than the charge/discharge cycle time ($>10^{-3}$ s), since the input capacitance levels are <100 pF. Hence, charging time does not in practice place a limit on the extent to which $C_{\max}$ can be increased.

III. Capacitance Optimization

Since capacitance is the key parameter for maximizing ΔE, a comprehensive capacitance analysis has been performed. The focus is to increase $C_{\max}$ because previous prototypes exhibit

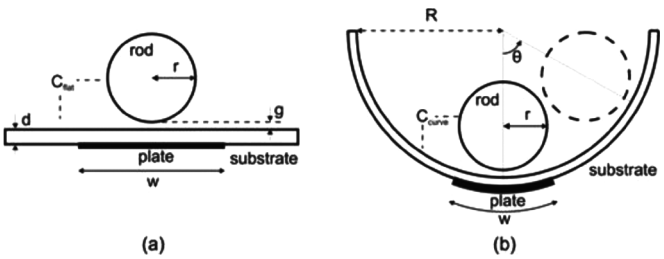

Fig. 5. Definition of geometrical parameters for (a) flat substrate and (b) curved substrate rolling rod electrostatic harvesters.

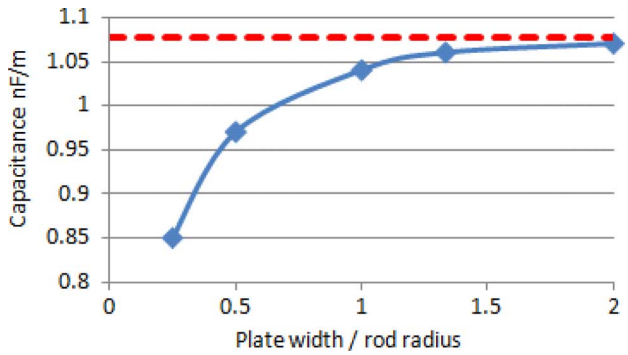

Fig. 6. Simulation of rod-plate capacitance versus the ratio of the plate width over the rod radius, for the planar substrate case. The dashed line represents the analytical value calculated from (3) for an infinite plate width. An air gap of 1 μm is assumed.

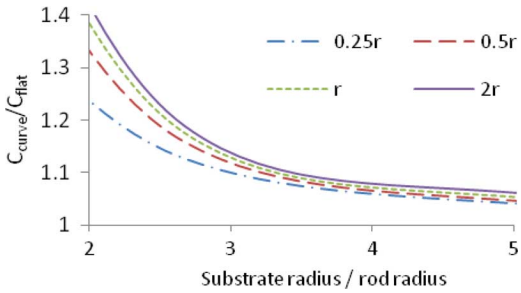

Fig. 7. Normalized capacitance versus the ratio of the substrate radius over the rod radius for four different plate widths.

a $C_{\min}$ value approaching the parasitic value. It would be undesirable to reduce this further due to the loss of design predictability in terms of gain. The analysis begins by considering the case of a flat substrate. Fig. 5(a) shows the geometry for this case. The rod-plate capacitance per unit rod length depends on several parameters: the rod's radius r, the thickness of the isolation layer d, the plate width w, and g, which is the minimum air gap between the rod and film caused by surface roughness and nonstraightness of the rod. The minimum possible separation of the electrodes, and therefore maximum possible capacitance, is determined by the thickness of the SiO_2 dielectric layer and the air gap. The dominating factor in our prototype is in fact g.

The first parameter to be investigated is w. If the width is infinite, capacitance will be maximal, all else being equal. Using the image plane method [21], the capacitance between two parallel rods can be treated as equivalent to two identical rod to infinite plate capacitors in series. From (3) is derived to give the rod plate capacitance per unit length analytically, assuming w is infinite

$$C = \frac{2\pi\varepsilon_0}{In\left(1+\frac{g}{r}+\sqrt{\left(\frac{g}{r}\right)^2+2\frac{g}{r}}\right)}. \tag{3}$$

Fig. 6 compares the capacitance determined numerically using the finite element software, Ansys (solid line) to model the geometry of Fig. 5(a), with the theoretical capacitance for infinite plate width (dashed line) given by (3). This shows that the numerically determined capacitance increases rapidly as w/r increases such that beyond $w/r \approx 1.33$ the capacitance is within 2% of the theoretical value for infinite w/r. For practical designs, equation (3) will normally be applicable, since it is desirable to maximize $C_{\max}$. The protopype uses $w = 1000\ \mu$m and $r = 750\ \mu$m.

Capacitance is proportional to the rod's radius and inversely proportional to air gap, assuming the radius is much bigger than the air gap, which is likely to be the case in any practical design. In the prototype, $r = 750\ \mu$m and $g \approx 1\ \mu$m. The capacitance is expected to be around 10 pF for a 1 cm long rod and a value of around 8 pF was measured. The air gap is determined by the surface roughness of the dielectric layer and the rod's straightness which, in fact, dominates over the isolation layer d. Therefore, not only is it important to produce the thinnest isolation layer possible (while not causing electrical breakdown) but also the flattest. A motivation for using the conformal plane structure, shown in Fig. 5(b), is the expectation of enhanced capacitance, $C_{\max}$, due to the ground plate being closer to the rod surface. Numerical analysis has been used to determine the degree of curvature required to achieve a certain capacitance increase compared to the value determined by (3). These figures can be weighed up against other considerations to determine the optimal degree of curvature.

Fig. 7 plots the capacitance ratio $(C_{\text{curve}}/C_{\text{flat}})$ versus the radius ratio (substrate over rod, R/r) for four different plate widths. The results are normalized based on extrapolation from numerical analyses; this extrapolation has been inferred but not proven rigorously. A 1 μm air gap was applied for all simulations. Fig. 7 enables the designer to predict the extent to which the capacitance given in (3) for a flat substrate can be increased by curving the substrate.

It might be concluded that the optimal design would involve a very high degree of curvature, with the substrate radius approaching the rod radius, since this would yield the largest $C_{\max}$. The rod must, however, travel the distance necessary to have multiple charge-discharge cycles during movement in one direction. This is for two reasons. First, the energy generated is proportional to the number of charge-discharge cycles for a given excitation frequency. Second, the new architecture relies on a passive method to identify the sensor. The proposed approach is to vary the distance and therefore the time between discharge pulses, hence creating a unique code for each sensor. The number of charge-discharge contacts achievable is limited by the plate width needed for maximum capacitance $w = 1.33r$ and the distance of travel required to achieve the maximum capacitance change. The latter is about 100 μm for the flat substrate device [21]. To illustrate the tradeoff, R/r should be

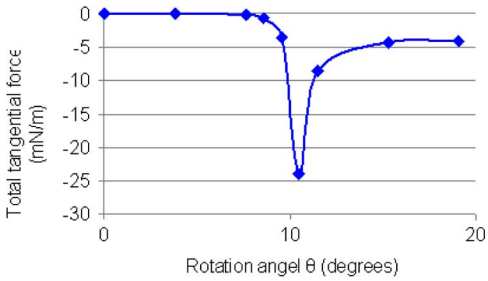

Fig. 8. Electrostatic force in the tangential direction versus rotation angle.

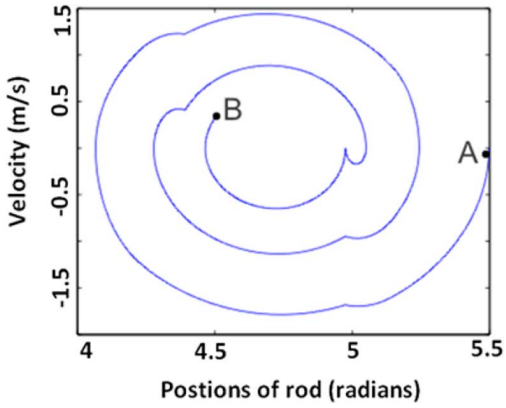

Fig. 9. Velocity of rod versus position. The position is described by the angle in radians. The lowest point in the arc has position 1.5π or 4.71 rad. The rod is released under gravity from position A (5.5 rad) and stopped at position B, where it is held by electrostatic force over one of the bottom electrodes.

greater than 2 to achieve more than four discharge pulses for a rod radius of 750 μm if both the capacitance ratio and the rod-to-plate capacitance are to remain maximal.

It should be noted that $C_{\min}$ is also boosted by substrate curvature. $C_{\max}$ nonetheless benefits to a much larger degree because the overlap between the rod and the plate is far larger at the charging (maximum capacitance) point.

The radius of our prototype device varies in fact between $2r$ and $4r$ since it is not uniform, i.e., the substrate is not perfectly circular. The average measured capacitance increase was a factor of 1.5: 8 pF for a flat substrate and 12 pF for a conformal substrate. It is higher than predicted in Fig. 11 due to the SiO_2 layer thickness being marginally less in the conformal case. The device generates 4.7 times as much energy as the flat plane prototype.

IV. Dynamic Analysis

A. Electrostatic Force

The electrical energy converted, i.e., the energy output, is the integral of the electrostatic force between the rod and bottom electrode over the traveling distance. The features of this force are thus crucial for maximizing generated energy and improving energy conversion efficiency. An excessive force will freeze the rod at its charging location and prevent it from rolling, while an inadequate force yields less energy output. Designing the optimal force needs to consider the dominating maximum acceleration experienced by the rod. Fig. 8 plots the Ansys simulated results of the electrostatic force versus rotation angle, where the 2D model used for the simulation is shown in Fig. 5(b).

The force appearing negative in Fig. 8 represents its nature as an impeding force. The peak magnitude is close to 250 μN. Comparing this to the weight of a 1 cm long 1.5 mm diameter steel rod (1.3 mN), the electrostatic force is capable of withholding the rod until the acceleration applied exceeds approximately $250/1300 \cdot 9.8 = 1.9$ m/s^2, or about 0.2 g. This value will of course depend on the priming voltage.

The effect of electrostatic force on the movement of the rod is clearly seen in the numerical simulations (Fig. 9). The sudden changes in the curvature of the traveling path indicate the electrical energy extracted at those positions.

B. Sliding and Rotation

A moving rod could experience two types of motion: rolling only and combined sliding and rolling, depending on the frictional coefficient between the rod and substrate and the acceleration acting on the rod. Excessive sliding would wear out the thin SiO_2 isolation layer rapidly. As a result, it is beneficial to confine the rod to the rolling only mode.

In the case of the flat substrate architecture shown in Fig. 5(a), the boundary condition between rotational and sliding-rotational motion can be calculated from the corresponding equations of motion. For only rotational motion, the overall rod acceleration equals the angular acceleration: $a = r \cdot \partial\omega/\partial t$, where r and ω are the rod's radius and angular velocity, respectively. The two forces acting on the rod are the inertial force $F_i = m \cdot a_{\text{ext}}$ and the static friction force F_f, where m and a_{ext} are the rod mass and the external acceleration, respectively. The difference between the two forces should equal the total acceleration times m : $F_i - F_f = ma$. In addition, since the only torque applied to the rod is the one of the friction force, we have $F_f \cdot r = I \cdot \partial\omega/\partial t$, where $I = 0.5 \cdot m \cdot r^2$ is the rod's moment of inertia. From these equations, we see that during rotational only motion, the static friction force is equal to one third of the inertial force

$$F_f = \frac{F_i}{3}. \tag{4}$$

The motion mode change occurs if F_f exceeds its maximum value: $F_f = \mu_0 \cdot m \cdot g$, where μ_0 is the static friction coefficient and g is the gravitational acceleration. Hence, the maximum external acceleration for rotational only motion is found to be equal to $3 \cdot \mu_0 \cdot g$. If the motion source is a vibration of angular frequency ω_0 and amplitude Y_0, then its maximum acceleration is $\omega_0^2 \cdot Y_0$ and the condition for rotational only motion becomes

$$\omega^2 Y_0 = 3 \cdot \mu_0 \cdot g. \tag{5}$$

Fig. 10(a) illustrates the boundary between the two motion modes. To the left of the lines only rotation occurs; to the right rotation and sliding will take place.

In the case of the conformal substrate architecture shown in Fig. 5(b) (driving source is initial elevated angle), the boundary condition is described by (6), where θ_0 is the elevated angle

$$\theta_0 = \arctan(3\,\mu_0). \tag{6}$$

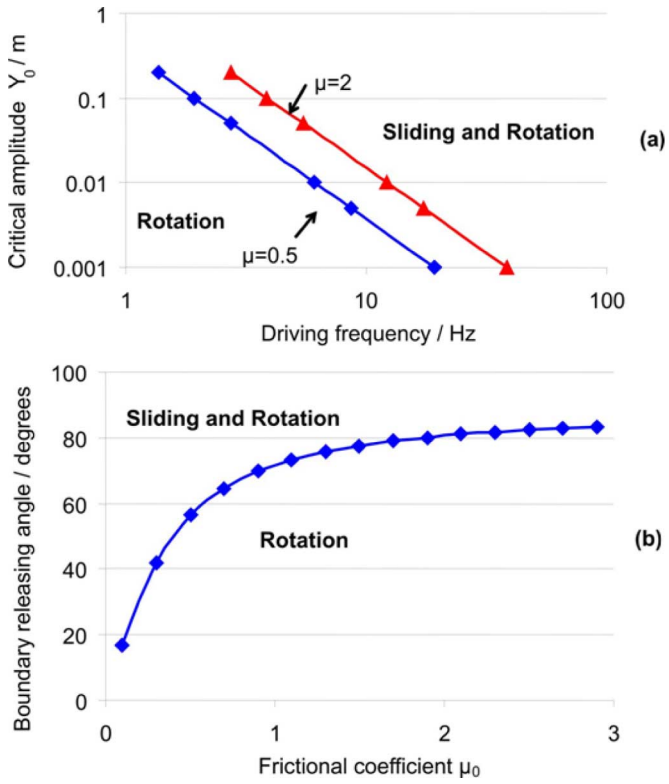

Fig. 10. (a) Motion mode boundaries for two different friction coefficients. In the area below each line, purely rotational motion occurs. In the area above each line, a combination of rotational and sliding motion is expected. (b) Simulation of the rod angular position at which motion mode change occurs versus friction coefficient. Pure rotation occurs in positions lying below the line.

Fig. 10(b) illustrates the relationship graphically. If the release angle is greater than the boundary values, i.e., above the curve, the rod will experience combined rotation and slip motion. For typical values of μ for glass-to-metal contact of 0.5–0.7, a high angular range of ± 55–65° can be exploited without slip.

V. Fabrication

The MEMS microgenerator is fabricated using a flexible 75 μm thick polyimide film to allow substrate curving. The first step is to cut the film into a 10 mm diameter circle and bond it onto a standard 100 mm borofloat glass wafer. The bonding is implemented by evenly taping the perimeter of the polymer circle onto the wafer with Kapton film. The purpose of the glass wafer is to support the soft substrate through the fabrication. It is removed at the end of the process.

Next, three layers are sputtered onto the polymer. They are 30 nm of Cr for better adhesion, 300 nm of Cu as the bottom electrode, and 50 nm of SiO_2 as the dielectric layer. Photo resist (PR) spinning (Shipley Microposit S1828) is implemented immediately after sputtering to minimize oxidation on the Cu surface. Then, the wafer undergoes UV exposure and development.

Next, using the PR film as a mask, the exposed SiO_2 layer is patterned by reactive ion etching (RIE). Then, the wafer is rinsed in plating solution before 3 min of Cu electrodeposition. The deposition current is precalculated to ensure a 100 nm thick Cu layer. The height of the contacts is elevated to ensure successful electrical contact with the rod.

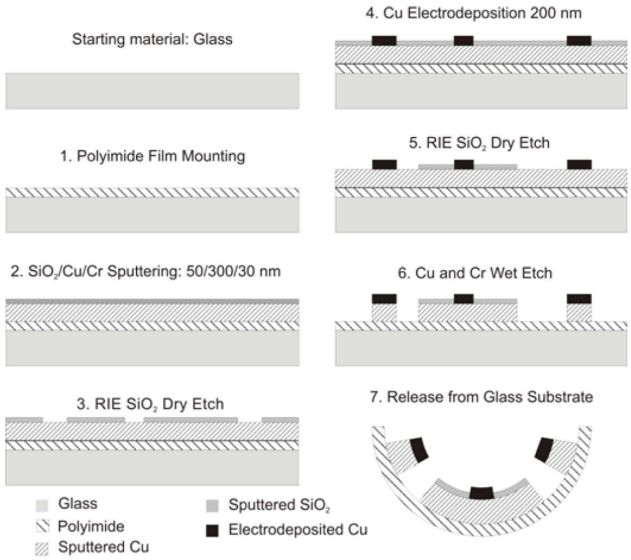

Fig. 11. Fabrication process of the energy harvesting device.

The remaining resist mask is then removed with acetone. The second lithography process employs the same method to form the contacts and bottom plates. Then, SiO_2 etch is carried out by RIE as before. This is followed by removal of sputtered Cu and Cr with chemical wet etch. The last step is to soak the wafer in acetone to strip off any residual PR. The supporting glass wafer can be removed either before or after the PR stripping.

Single die were cut off, bent into arc shapes and taped to maintain their curvature. Through-film bonding is employed to facilitate electrical connections (shown as grounding vias in Fig. 4). The generator is then mounted onto a test board, shown in Fig. 12(a), which includes the single turn loop antenna for transmission, an electrical connector to apply the priming voltage, and instrumentation combined with a SMA output for connection to an oscilloscope for characterization. The single-turn copper wire loop antenna was chosen to be 3 cm in diameter to achieve a reasonable Q-factor, while achieving good radiation efficiency in the low UHF region.

VI. Measurement Results

The contact resistance between the rod and the electrodes was measured to be less than 1 Ω. A physical characterization of such contacts can be found in [22].

The voltage gain (output voltage divided by priming voltage) for different priming voltages applied to the conformal substrate device was measured and is shown in Fig. 13. From this the consistency of the gain can be assessed, which is important since accurate readings depend on linear and repeatable behavior. The prototype results indicate that the voltage gain is consistent within about 15% of the maximum value over almost a 10 V range. Gain deviation may be due to capacitance ratio mismatch between charge-discharge cycles caused by variation in the substrate curvature and variations in rod and substrate flatness.

The voltage gain G, is related to the energy gain ΔE as

$$\Delta E = \frac{1}{2} V_{\text{prime}}^2 C_{\min} (G-1) G. \tag{7}$$

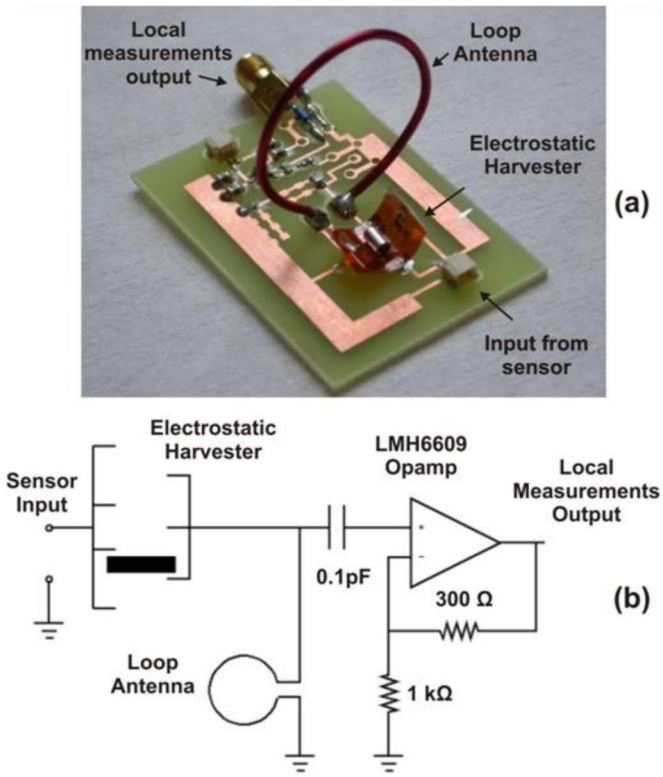

Fig. 12. (a) Optical image of the device test board. (b) Circuit model including electronics for measurement of the RF oscillation at the transmitter.

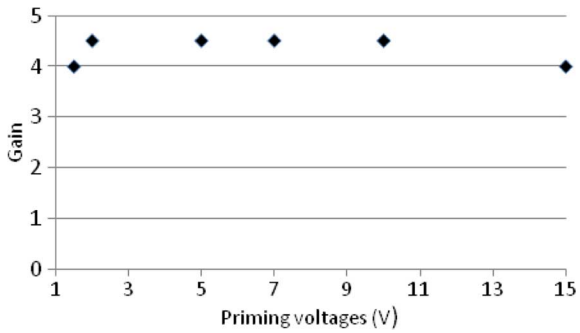

Fig. 13. Voltage gain versus priming voltage for the rod film prototype.

For large G, (7) can be approximated as

$$\Delta E = \frac{1}{2} V_{\text{prime}}^2 C_{\min} G^2. \tag{8}$$

A gain of 4.6 achieved for this conformal device compares favorably with the gain of 2.4 achieved with the flat substrate device published by the authors in [19]. This can be attributed to the use of a conformal substrate to increase $C_{\max}$ combined with improved fabrication techniques. For this gain, the $C_{\min}$ value of 1 pF and V_{prime} from 1 to 10 V, the transmitted pulse energies are in the range 10 pJ to 1 nJ.

An off-the-shelf UHF TV antenna connected directly to the high-speed scope was used to detect the transmitted signal wirelessly. Fig. 14 shows the successful reception at a range of 20 cm with a transmitted pulse energy of less than 50 pJ. As expected the signal is an exponentially decaying oscillation.

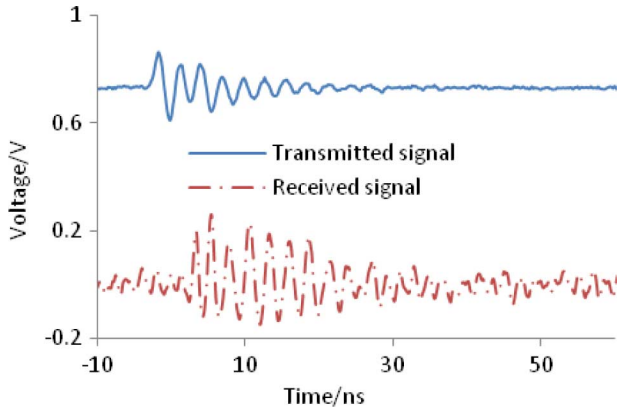

Fig. 14. Detection of oscillation for a pulse energy of 42 pJ.

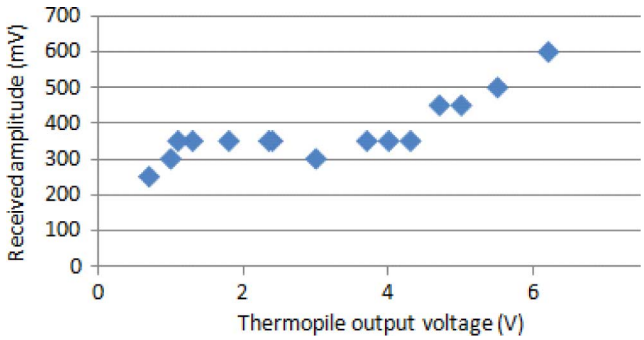

Fig. 15. Amplitude of received signal versus thermopile output voltage.

Equation (9) describes the decaying resonant pulse for a damped LC circuit

$$V = V_{\max} \exp\left\{-\frac{\omega}{2Q} t\right\} \cos(\omega t). \tag{9}$$

This was fitted to a number of transmitted and received signals to determine the both the resonant frequency and the Q factor. The transmitted signal can be detected directly using the test board's high frequency, very low input capacitance instrumentation amplifier connected to an oscilloscope [Fig. 12(b)]. The 100 fF series input capacitor is used to prevent the parasitic capacitance of the measurement circuit from significantly lowering the oscillation frequency. This circuit is useful when testing to compare transmitted and received signals. The frequency was found to be approximately 600 MHz and the Q was estimated to be about 20.

Both a pH sensor array as described in [23] and a thermopile [24] were used as sensors for the proof-of-concept self-powered wireless node. Successful RF signal transmission and reception was observed in both cases. Reliable detection was achieved for a range of up to 1 m for priming voltages down to 1 V. The received signal amplitude versus thermopile output voltage is shown in Fig. 15. The linearity is reasonable for the higher priming voltages, but the gradient decreases sharply below about 4 V.

VII. Discussion

The prototype battery-less self-powered wireless sensor node platform achieves successful wireless transmission over a range

of 1 m while harvesting only nanowatts of power. This demonstrates that the new architecture is indeed capable of operating at power levels orders of magnitude below conventional WSN nodes. However, certain enhancements would be necessary to enable the new wireless sensor platform to operate reliably in a real system. These are discussed next along with other possible improvements.

A. Generator

System gain nonlinearity and/or consistency are issues which require further development. It is important to solve this because reliable measurements will depend on the matching between charge-discharge cycles. As an example, the noncircularity of the substrate will result in varying generator gain depending on the charging contact. This can be solved through better assembly techniques. The nonstraightness and roughness of the steel rod and substrate should be improved for maximizing the energy output.

The current architecture is limited to operating with sensors which provide a voltage output. However, there are many such sensors, including piezoelectric devices for pressure and motion measurements, photoelectric light sensors, thermoelectric temperature sensors, and chemical sensors such as pH and glucose measuring electrodes. It should be noted that the architecture can potentially be modified to work with a capacitive sensor (such as a pressure sensor), which could form part of the resonant antenna network such that the transmission frequency would be modulated with the measured signal. In this case, the priming voltage would be provided by an electret or other fixed voltage source.

The experimental work showed that the curved substrate tends in itself to correctly control the motion of the rod. Nonetheless, additional features such as substrate trenches or side panels could also be used to prevent the rod from sliding out sideways.

B. Wireless Link

The loop antenna was designed to be large enough (3 cm diameter) to oscillate in the low UHF region for ease of testing. Next-generation devices will employ a much smaller antenna (below 1 cm diameter) and will resonate in the low GHz range. A node ID code can be included using different spacings between charge and discharge cycles. Calibration will be implemented by setting certain transmitted discharge pulses to a known reference amplitude, using either diodes or an electret. The development of a high sensitivity, high dynamic range receiver optimized for this application would also improve detection of the transmitted signal.

REFERENCES

[1] I. F. Akyildiz *et al.*, "Wireless sensor networks: A survey," *Comput. Networks*, vol. 38, pp. 393–422, 2002.

[2] Y. H. Chee *et al.*, "PicoCube: A 1 cm^3 sensor node powered by harvested energy," in *Proc. 45th ACM/IEEE Design Autom. Conf.*, Jun. 8–13, 2008, pp. 114–119.

[3] I. Stark, "Invited talk: Thermal energy harvesting with thermo life," in *Proc. Int. Workshop on Wearable and Implantable Body Sensor Networks*, 2006, pp. 19–22.

[4] I. Kuehne, M. Schreiter, H. Seidel, and A. Frey, "Optimum design of a piezoelectric MEMS generator for fluid-actuated energy harvesting," in *Proc. IEEE 24th Int Conf. Micro Electro Mechanical Syst. (MEMS)*, Jan. 23–27, 2011, pp. 1317–1320.

[5] D. A. Wang and K. H. Chang, "Electromagnetic energy harvesting from flow induced vibration," *Microelectronics J.*, vol. 41, pp. 356–364, 2010.

[6] S. Roundy and P. K. Wright, "A piezoelectric vibration based generator for wireless electronics," *Smart Mater. Struct.*, vol. 13, pp. 1131–1142, 2004.

[7] P. Glynne-Jones *et al.*, "An electromagnetic, vibration-powered generator for intelligent sensor systems," *Sens. Actuators A: Phys.*, vol. 110, pp. 344–349, 2004, 2004/2/1.

[8] S. P. Beeby *et al.*, "A micro electromagnetic generator for vibration energy harvesting," *J. Micromech. Microeng,.*, vol. 17, no. 7, pp. 1257–1265, 2007.

[9] P. Mitcheson *et al.*, "Energy harvesting from human and machine motion for wireless electronic devices," *Proc. IEEE*, vol. 96, no. 9, pp. 1457–1486, 2008.

[10] G. A. H. A.-R. Durou, A. Ramond, X. Dollat, C. Rossi, and D. Esteve, "Micromachined bulk PZT piezoelectric vibration harvester to improve effectiveness over low amplitude and low frequency vibrations," in *Proc. Power MEMS'10*, Leuven, Belgium, 2010, pp. 27–30.

[11] T. H. Ng and W. H. Liao, "Sensitivity analysis and energy harvesting for a self-powered piezoelectric sensor," *J. Intell. Mater. Syst. Structures*, vol. 16, pp. 785–797, 2005.

[12] N. G. Elvin *et al.*, "Feasibility of structural monitoring with vibration powered sensors," *Smart Mater. Structures*, vol. 15, pp. 977–986, 2006.

[13] P. Miao *et al.*, "Mems inertial power generators for biomedical applications," *Microsyst. Technol.*, vol. 12, pp. 1079–1083, 2006.

[14] H. Kulah and K. Najafi, "Energy scavenging from low-frequency vibrations by using frequency up-conversion for wireless sensor applications," *IEEE Sensors J.*, vol. 8, no. 3, pp. 261–268, Mar. 2008.

[15] [Online]. Available: http://focus.ti.com/lit/wp/slay015/slay015.pdfretrieved 11/04/11

[16] L. Huang *et al.*, "Ultra low power wireless and energy harvesting technologies; An ideal combination," in *Proc. IEEE Int. Conf. Commun. Syst, ICCS'10*, 2010, pp. 295–300.

[17] W.-J. Wu *et al.*, "Smart wireless sensor network powered by random ambient vibrations," in *Proc. IEEE Int. Conf. Syst., Man, Cybern.*, Taipei, Taiwan, 2006, pp. 2701–2708.

[18] D. C. Yates and A. S. Holmes, "Preferred transmission frequency for size-constrained ultralow-power short-range CMOS oscillator transmitters," *IEEE Trans., Circuits and Syst. I: Regular Papers*, vol. 56, pp. 1173–1181, 2009.

[19] C. He *et al.*, "MEMS energy harvester for wireless biosensors," in *Proc. IEEE 23rd Int. Conf. Micro. Electro. Mech. Syst., MEMS'10*, 2010, pp. 172–175.

[20] P. D. Mitcheson *et al.*, "Architectures for vibration-driven micropower generators," *J. Microelectromech. Syst.*, vol. 13, pp. 429–440, 2004.

[21] M. E. Kiziroglou *et al.*, "Rolling rod electrostatic microgenerator," *IEEE Trans. Ind. Electron.*, vol. 56, pp. 1101–1108, 2009.

[22] M. E. Kiziroglou, D. C. Yates, C. He, and E. M. Yeatman, "Body motion powered wireless transmission platform," in *Proc.. Power MEMS'10*, 2010, pp. 187–190.

[23] E. Bitziou *et al.*, "Simultaneous detection of pH changes and histamine release from oxyntic glands in isolated stomach," *Analy. Chem.*, vol. 80, pp. 8733–8740, 2008.

[24] Model TGM-287-1.0-2.5 retrieved 11/04/11. [Online]. Available: http://www.kryotherm.ru/?tid=47

Cairan He received the B.S. degree from Imperial College London, London, U.K., in 2006. Currently, he is working towards the Ph.D. degree in the Optical and Semiconductor Devices Group, Department of Electrical and Electronic Engineering, Imperial College London.

His research interests include microelectromechanical systems and energy scavenging for wireless sensor nodes.

Michail E. Kiziroglou (M'04) received the Diploma degree in electrical and computer engineering from Aristotle University of Thessaloniki, Thessaloniki, Greece, in 2000, the M.Sc. degree in microelectronics and nanoelectronics from Democritus University of Thrace, Xanthi, Greece, in 2003, and the Ph.D. degree in microelectronics and spintronics from the University of Southampton, Southampton, U.K., in 2007.

He is currently a Researcher with the Optical and Semiconductor Devices Group, Department of Electrical and Electronic Engineering, Imperial College London, London, U.K. His research interests include novel microelectromechanical systems, semiconductor integration, and nanoelectronic devices.

David C. Yates (M'03) received the M.Eng. degree in electrical engineering and the Ph.D. degree from Imperial College London, London, U.K., in 2001 and 2007, respectively. His doctoral research focused on ultra-low-power wireless links.

He is currently a Research Associate with the Optical and Semiconductor Devices Group, Department of Electrical and Electronic Engineering, Imperial College London. His research interests include low voltage and low-power analog and RF circuits and systems for body sensor networks.

Eric M. Yeatman (M'01–SM'05) received the B.Sc. degree from Dalhousie University, Halifax, NS, Canada, in 1983, and the Ph.D. degree from Imperial College London, London, U.K., in 1989.

Since 1989, he has been a Member of Academic Staff in the Department of Electrical and Electronic Engineering, Imperial College London, where he is currently a Professor of Microengineering and Deputy Head of the Department. His research interests include micromechanical actuators and generators, microstructures for optical and radio frequency applications, and technologies for pervasive sensing.